DESIGN AND FLOW ANALYSIS OF SWEPT BACK WING

DEN318 – THIRD YEAR PROJECT – TECHNICAL REPORT- 2022/23

PREPARED BY,

SURAJ PATEL

200287263

SUPERVISED BY,

DR. ELDAD AVITAL

25/04/2023

SCHOOL OF ENGINEERING AND MATERIAL SCIENCE 2023
DECLARATION

This report entitled,

"DESIGN AND FLOW ANALYSIS OF SWEPT BACK WING ON CIVIL AIRCRAFT"

Was composed by me and is based on my own work. Where the work of the others has been used, it is fully acknowledged in the text and in captions to figure illustrations. This report has not been submitted for any other qualification.

Suraj Patel: …………………….

Date: ……………………..

ACKNOWLEDGEMENT

ABSTRACT

The 18.1° root to tip sweep, NASA SC(2)-0410 airfoil profile wing model is considered in this project for flow investigation. The experimental method takes place in low-speed wind tunnel by placing tufts attached wing model in, also, the variation of the angle of attack and different speeds range has been set for the experiment. The angle of attack increment with high speeds induces a three-dimension vortex structure at the wing tips of the model and creates spanwise flow due to sweep angle. The numerical methods: lifting line theory and vortex lattice of the computational fluid dynamic software XFLR5 utilized to validate the experimental results. Prior to that, 2D object meaning airfoil has been taken into account to understand better flow structure over the wing since some theories produce higher accuracy results for 2D objects. The low Reynolds numbers operation are desired to analyse for this report.

Keywords: *Swept-back wing, flow-visulisation, computational fluid dynamics, XFLR5*

TABLE OF CONTENTS

LIST OF FIGURES

1. INTRODUCTION

The birds, whales and many aquatic animals have their wing backward than the straight. This question is raised when the object deals around fluids. There is not wrong to say if the swept wing concepts are derived from nature. The swept wing application was introduced just before the end of World War II. The wing sweep has the characteristics to delay onsite formation of shockwave. As the oncoming flow velocity splits into two components at the leading edge of the wing, normal and spanwise. The normal component of the velocity causes the shock wave formation. However, further research also shows reduction in drag by applying sweep angle. The shock wave formation costs induced flow separation and eventually increased total drag. The shockwave on the wing is series of the wave accumulated at the certain point on the wing that point is considered as the critical Mach number where the Mach number is 1 and flow then trail through subsonic environment. Thus, the choice of the sweep angle on the wing is optimized carefully.

For this project, NASA SC(2)-0410 airfoil profile wing is chosen to investigate flow characteristics over it. An experimental approach will be adopted to analyse the flow-pattern. Also, the computational fluid dynamics method will be considered to validate the empirical results.

2. LITERATURE REVIEW

Adolf Busemann was the first one who introduced the concept of the swept wing at fifth volta conference in 1935. Busemann remarked that the normal velocity component of the oncoming speed become dominate of the freestream velocity. [1] In 1939, Hubert Ludwieg conducted the first wind tunnel test to evaluate Busemann's theory.[2] The experiment was carried out with two wings, straight wing (i.e., zero sweep) and 45 degree swept wing in transonic regime. The results of that experiment proved the swept wings offer drag reduction. Those results were also shared with Albert Betz and Willy Messerschmitt in later 1939. Willy then made German jet-powered Messerschmitt Me 262 and rocket-powered Messerschmitt Me 163. Unfortunately, both aircraft suffered from compressibility effects and uncontrollable at high speeds. In the decade of 1930s and 1940s many research and investigation carried on the sweep theory out of which NACA's Robert T. Jones breakthrough study emerging out on effect of sweep back on boundary layer and separation in 1947.[3] In 1954, Haines did study on the swept wing with lower Mach Number (~0.5 to 1) and noticed that the part-span vortex sheet originated from near the leading edge inboard end of the separation and pass across the span of the wing.[4,6] The 21st century works in the swept back subject, inconsistencies in Busemann's simple sweep theory has presented by Takahasi, Kady and Dulin in 2014 AIAA aviation conference.[7,9] They also represented the solution of those inconsistencies by employing modern CFD in 2015 AIAA aviation conference.[8,9]

3. METHODOLOGY

The fluid-flow can be analysed in various ways such as theoretically, numerical computationally, and experimentally. The fluid-flow visualisation is troublesome due to its invisibility. Several methods such as optical (refractive index, schlieren, shadowgraph), wall trace (tufts, evaporative and chemical, surface oil), and marker (dye or smoke, surface powder, hydrogen bubble) can be utilized for flow-visualisation.[10] The flow-visualisation can be directly observed or captured in a video camera by applying these methods to an aerodynamic object. Experimentally, the wall trace tufts attached method is used to analyse flow for this project. Prior to that, the 3D cad model of NASA SC(2)-0410 airfoil profile wing must be manufactured to apply this method on.

Moreover, mathematical computational methods are comparatively much cheaper than most of the above-mentioned methods, therefore, computational fluid dynamic (CFD) software XFLR5's preliminary results are also included to validate the experimental data. XFLR5 has four methods of flow analysis, out of which two methods (1) non-linear lifting line theory and (2) vortex lattice are considered for this project. The lifting-line theory is viscous, but VLM is inviscid.[11] The additional explanation and understanding are reviewed in their respective sections.

3.1 Experimental Analysis Methodology

The indispensable part of the project to evaluate the aerodynamics of the swept-back wing is accomplished by conducting an experiment in a subsonic wind tunnel. This open-return wind tunnel structure is shown in Figure 1 schematic diagram.
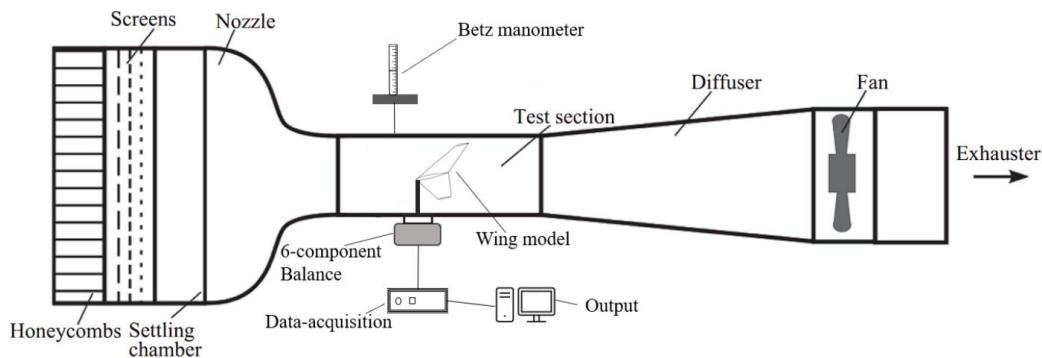
Figure 1: Schematic Diagram of the subsonic wind-tunnel[12]

The wind tunnel consists of the 7 main sections: Noise and onflow turbulence intensity reduction area, settling chamber, nozzle, test section, development chamber (diffuser)[13], blower fan, and exhauster. The test section dimensions of this wind tunnel are 1000mm height with 1220mm width. The achievable speed range in this wind tunnel is from 0m/s up to 40m/s and is controlled by the Betz manometer setup attached to the working section of the tunnel. The NASA SC(2)-0410 airfoil profile wing model was fabricated in a 3D printer using the PTE material.

Afterward, the model was followed by the polishing process. The tufts attachment on the polished wing model delivers better flow visualisation. The 18-degree root-to-tip wing-sweep, tufts attached, polished wing model placed on the traverse mechanism in the working section of the open-circuit wind tunnel as shown in Figure 2.

2

Figure 3: Schematic Diagram of the NASA SC(2)-0410 airfoil profile wing model with accurate dimension

Figure 2: The tufts attached NASA SC(2)-0410 airfoil profile wing model placed in the test section of the open-circuit wind-tunnel. (*The picture was taken from the side of the wind tunnel as both sides of the wind tunnel are covered with transparent plexiglass for flow-visulisation.*[17])

The 6-component balance measures all the values for three forces (lift, drag, and side) and three moments (pitch, roll, and yaw) for the model in test-sectio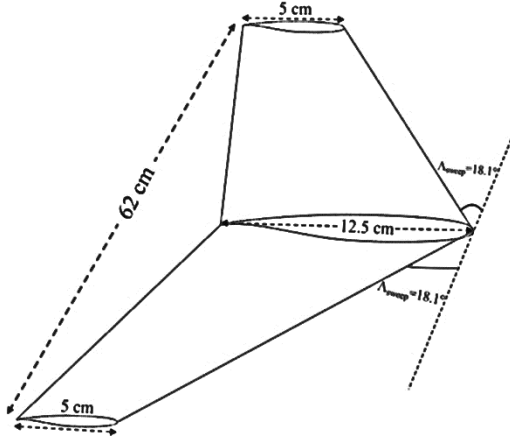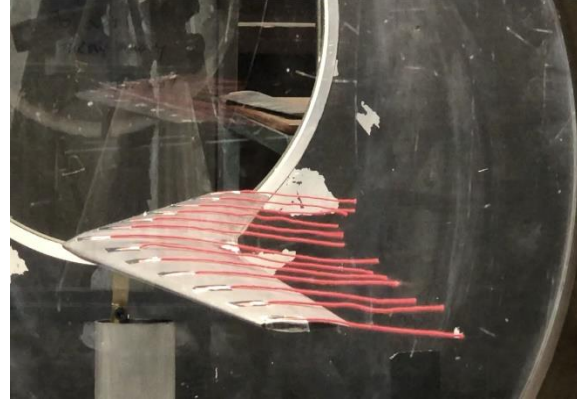n during the experiment. The values thereafter retrieved by data acquisition to output source for analysis. The entire experiment was carried out at the Reynolds number range from 62000 to 220000. The fifteen various angles of attack (α) and eight different freestream velocities (V_∞) were considered for this experiment, ranging from -5° to +20° and 17.33m/s to 35.13m/s respectively.

The atmospheric conditions are considered as,
Temperature: T_{atm} = 18.233 °C
Pressure: P_{atm} = 1016.35 hPa
Density: ρ = 1.2113 kg/m^3
Dynamic viscosity: μ = 1.80494 × 10^{-5} Pa.s
Kinematic viscosity: ν = 1.4854 × 10^{-5} m^2/s
Mean Aerodynamic Chord (MAC): d_{MAC}: 9.2857 cm

The acquired values from the experiment for analysis will be discussed in the subsequent sections.

3.2 Computational Fluid Dynamics Analysis – XFLR5

Computational Fluid Dynamics is all about solving the Navier-Stokes equation numerically. For this project, the CFD analysis of the identical swept-back wing model was performed in XFLR5 (v6.57_win64) software. In XFLR5, the flow analysis output offers results based on the Navier-stokes equation. Therefore, sometimes it is also referred as the Reynolds Averaged Navier-stokes solvers (RANS).[14]

The Navier-stokes equation is made easy by splitting in the inviscid and time-averaged turbulence part. The viscosity is omitted from the inviscid part of the equation, also, the theory is preferably applied for high Reynolds number flows and low angle of attack flow where flow separation would not be a case. Thus, it is introduced as the potential flow.[15] On the other hand, the time-averaged

3

turbulence is entrenched on Reynolds equation. The viscosity, uniform pressure in boundary layer thickness, and Prandtl mixing length hypothesis are considered in the tertiary (3d) boundary layer equation. By deriving it twice, the equation ended up with a linear boundary layer integral equation and a secondary boundary layer differential equation. XFLR5 generates interpolated second-order viscous results out of the diverse empirical and theoretical results including turbulent and transition models. This entire process is also known as Reduced Order Modelling which illustrates in this case reducing the order of the equation to obtain results more simply. The non-linear lifting-linear theory and vortex lattice methods are useful to analyse the flow, and both work on the same principle of classic LLT theory.[14]

3.2.1 XFLR5: Lifting-line Theory - (Non-Linear)

This theory was first described by Frederick W. Lanchester in 1907 and in 1918-1919 by Ludwig Prandtl. The Lanchester-Prandtl lifting-line theory is a numerical method to estimate lift distribution over a 3D wing from the wing's geometry.[20] The theory is based on the hypothesis that a lifting wing can be assumed as a lifting line (*basically neglecting the thickness of the wing*) and also assumed the vortices formation along the span trial consider in the freestream velocity direction in a straight line. The classic lifting-line theory is linear. The viscous effects are neglected in linear LLT.

However, at some point, the wing's profile lift curve is not linear, particularly at the high angle of attack, where an analytical solution cannot be viable. At that point, the non-linear method proves useful to estimate lift distribution. The non-linear lifting-line theory is viscous and then can be interpolated with the data of the second-order viscous results from airfoils (*XFOIL*) to provide an estimation of the lift production.[19]

$$\Gamma(y) = \frac{1}{2} V_\infty \, c_n \, c_l(y_n)$$

The above equation of the circulation $\Gamma(y)$ where V_∞ is the freestream velocity, c_n is the chord length at each point on the wing and c_l is the lift coefficient at that point.[19]

$$C_L = \frac{2}{V_\infty \, S} \int_{-b/2}^{b/2} \Gamma(y) \, dy$$

The coefficient of lift equation is mentioned above where S is the wing area and b is the total length of span. (i.e., *b = 2s*)

The non-linear lifting-line theory cannot provide precise results of the wings with a low-aspect ratio and high sweep angle. In addition, the wing's planform presumed to lie on the X-Y plane implies the dihedral angle is negligible.[15]

3.2.2 XFLR5: Vortex lattice Method - (Linear)

This method's background was presented by John DeYoung in the NASA Langley workshop. The Vortex lattice method (VLM) is the extension of the Lanchester-Prandtl lifting-line theory. In the computational fluid dynamics (CFD) world, this numerical method is predominantly utilized in the early phase of aircraft designs and aerodynamic applications. The flow-field in VLM is

inviscid, incompressible, and linear. The calculation of the aerodynamic quantities is independent of the air's viscous characteristics and the wing's freestream velocity. The basic fundamental of this method is to sum vortices from each panel of the wing planform and model them into solitary vortices in the direction of the freestream velocity. The below equation suggests the vector cross product of the force acting on each panel, where ρ is the density of air, V_∞ is the freestream velocity and Γ is vortex strength.[11]

Figure 4: VLM method's Panels on wing planform surface in XFLR5

$$F = \rho \, V_\infty \times \Gamma$$

The lift coefficient equation for this method is illustrated by the below equation, where S is a sum of the panel's area and the force acting on each panel is F_z.[11]

$$C_L = \frac{1}{\rho \, S \, V_\infty^2} \sum_{panels} F_z$$

The VLM is restricted to a smaller angle of attack well before flow separation (i.e., stalled condition) as the VLM hardly interpolated values from the local lift coefficient. Thus, it is not recommended to consider results around stall angles of attack.[15]

4. RESULTS AND DISCUSSION

The aerodynamics quantities for this project derived from experimentally produces result as expected. The CFD results also have good agreement with the empirical values. The trends of results match with each other to a great extent despite the methods are viscous or inviscid. The experimental analysis is purely based on the real flow where all necessary viscous effects exist. However, XFLR5 theories have different approaches towards the viscosity that have already been studied in methodology.
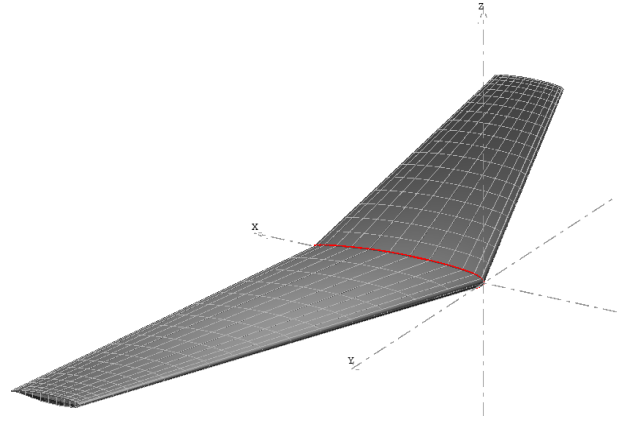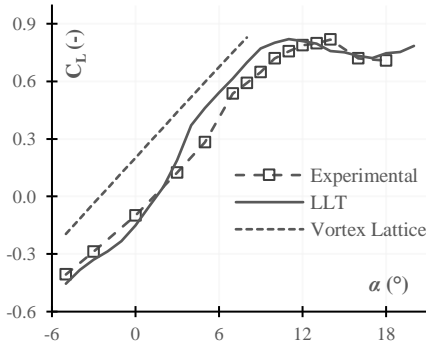

Figure 5: Lift coefficient against AoA, Re = 108,000 (V_∞=17.33 m/s)
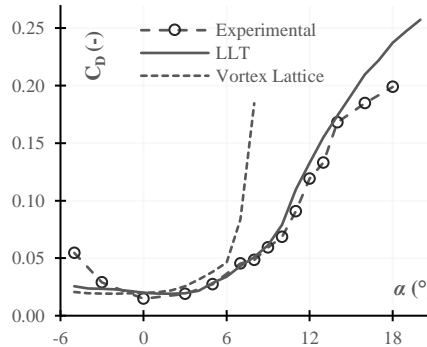

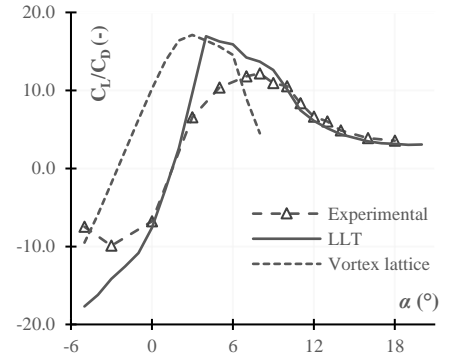Figure 6: Drag coefficient against AoA, Re = 108,000 (V_∞=17.33 m/s)

Figure 7: Lift-to-drag ratio against AoA, Re = 108,000 (V_∞=17.33 m/s)
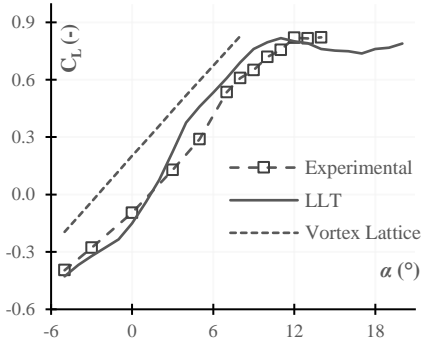
Figure 8: Lift coefficient against AoA,
Re = 125,000 ($V_∞$=20.01 m/s)
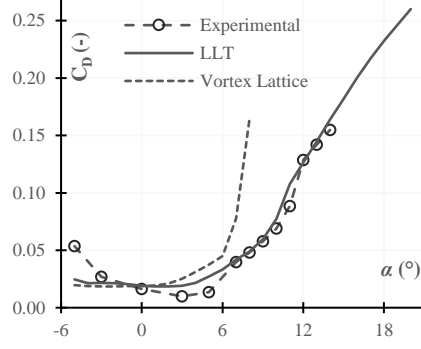

Figure 9: Drag coefficient against AoA,
Re = 125,000 ($V_∞$=20.01 m/s)
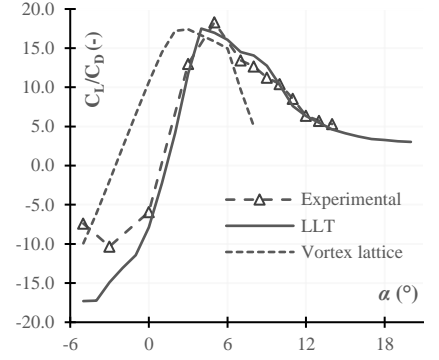

Figure 10: Lift-to-drag ratio against AoA,
Re = 125,000 ($V_∞$=20.01 m/s)

Figure 11: Lift coefficient against AoA,
Re = 144,000 ($V_∞$=23.102 m/s)

Figure 12: Drag coefficient against AoA,
Re = 144,000 ($V_∞$=23.102 m/s)

Figure 13: Lift-to-drag ratio against AoA,
Re = 144,000 ($V_∞$=23.102 m/s)

Figure 14: Lift coefficient against AoA,
Re = 157,000 ($V_∞$=25.175 m/s)

Figure 15: Drag coefficient against AoA,
Re = 157,000 ($V_∞$=25.175 m/s)

Figure 16: Lift-to-drag ratio against AoA,
Re = 157,000 ($V_∞$=25.175 m/s)
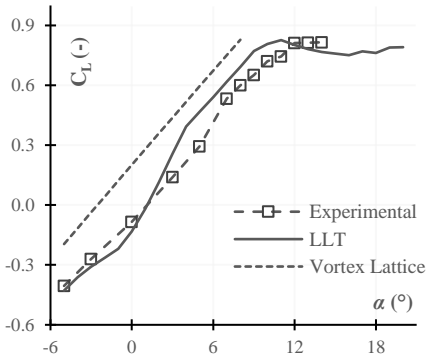
Figure 17: Lift coefficient against AoA,
Re = 169,000 (V_∞=27.09 m/s)
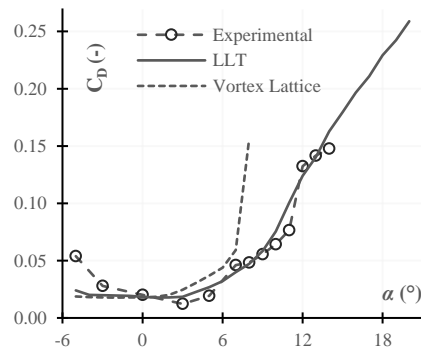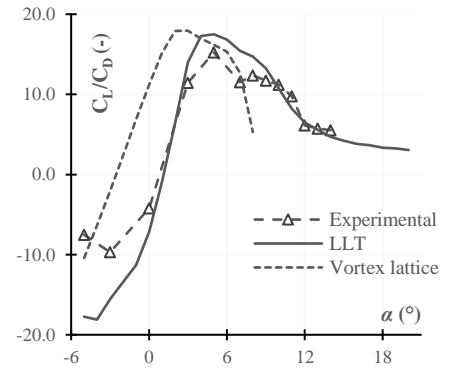

Figure 18: Drag coefficient against AoA,
Re = 169,000 (V_∞=27.09 m/s)

Figure 19: Lift-to-drag ratio against AoA,
Re = 169,000 (V_∞=27.09 m/s)

Figure 20: Lift coefficient against AoA,
Re = 187,000 (V_∞=30.01 m/s)

Figure 21: Drag coefficient against AoA,
Re = 187,000 (V_∞=30.01 m/s)

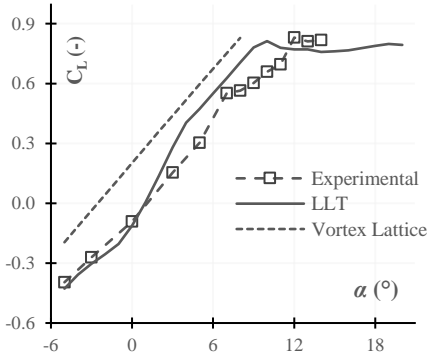Figure 22: Lift-to-drag ratio against AoA,
Re = 187,000 (V_∞=30.01 m/s)

Figure 23: Lift coefficient against AoA,
Re = 207,000 (V_∞=33.18 m/s)
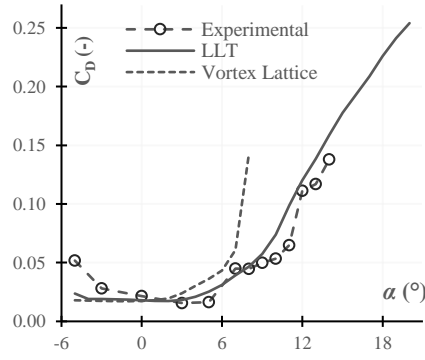

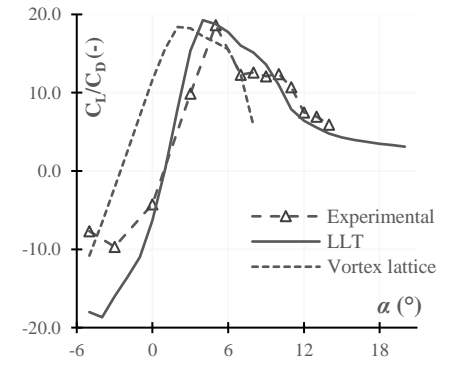Figure 24: Drag coefficient against AoA,
Re = 207,000 (V_∞=33.18 m/s)

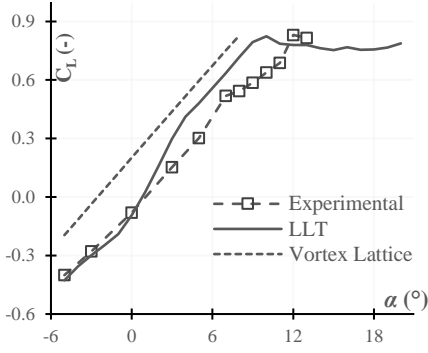Figure 25: Lift-to-drag ratio against AoA,
Re = 207,000 (V_∞=33.18 m/s)

Figure 26: Lift coefficient against AoA, Re = 219,000 (V_∞=35.13 m/s)
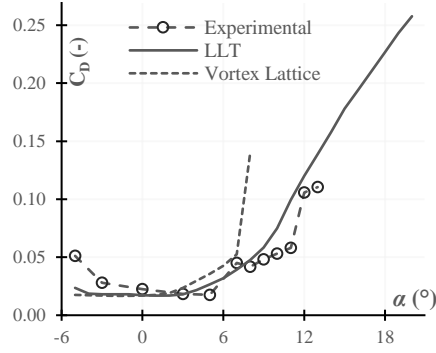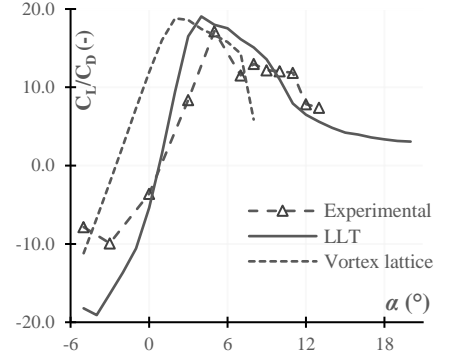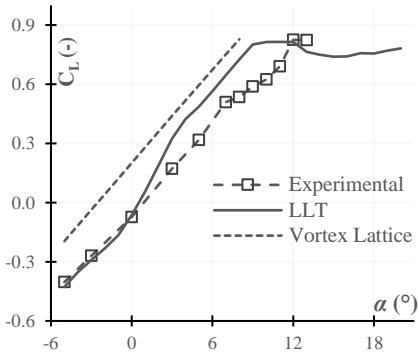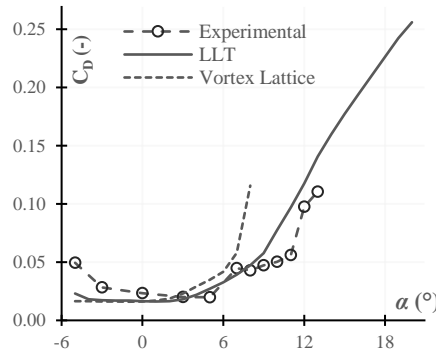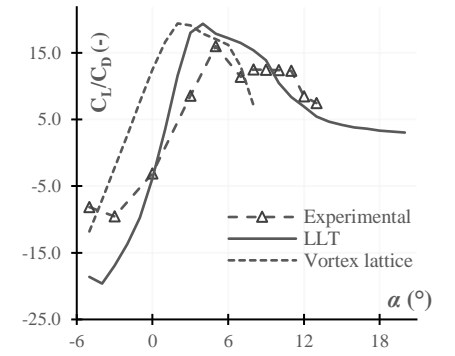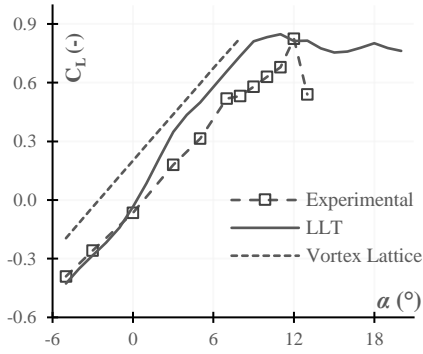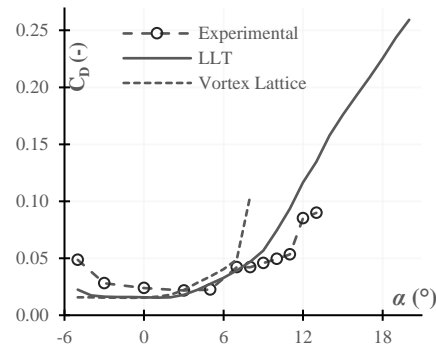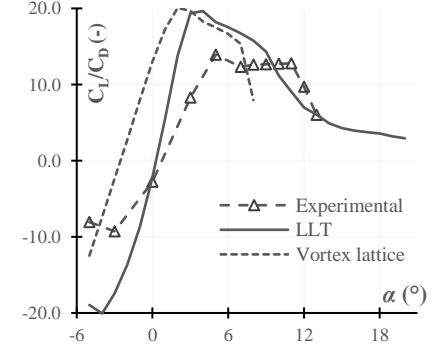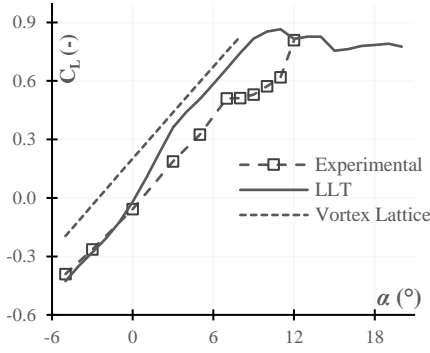
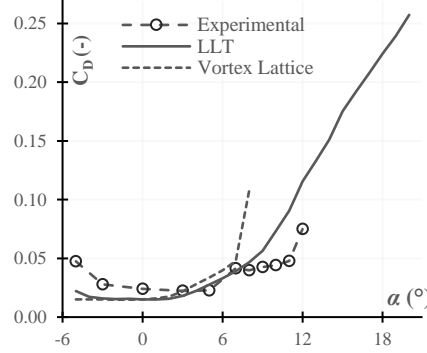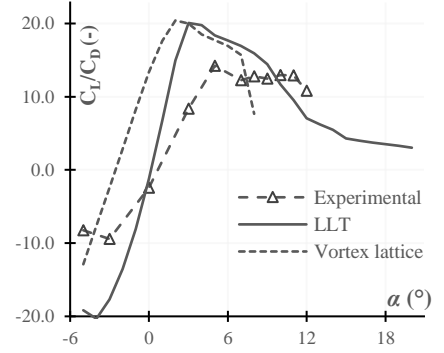Figure 27: Drag coefficient against AoA, Re = 219,000 (V_∞=35.13 m/s)

Figure 28: Lift-to-drag ratio against AoA, Re = 219,000 (V_∞=35.13 m/s)

The coefficient of lift values from the experiment has an identical trend with each configuration of the Reynolds number. The non-linear lifting line theory's lift coefficient graph showcased the presence of the viscosity at the 1-degree angle of attack to 4- degree angle of attack as the sudden increase in the graph at that region. The vortex lattice method is only able to provide estimation well before the stall region as this method's algorithm first calculate local lift coefficient Cl value and based upon that further interpolation with second order viscous drag considered with the local Cl. However, this method raises an issue for high and low value of Cl and polar can only be interpolated either before the stall angle or after the stall angle. In this case, the values are only interpolated to the 8-degree angle of attack which is well-before the stall angle. The XFLR5 flow running analysis then shows the error message for the rest of angles of attack configuration as *"The value could not be interpolated."*

The drag coefficient against angle of attack graphs has good estimation match with each method. As discussed before, the non-linear lifting line theory has predicted the drag coefficient values as expected but vortex lattice method has raised same issue as previously since the flow analysis run parallelly for each necessary aerodynamic quantity.

The lift-to-drag coefficient graph implies a lift-to-drag ratio against angle of attack. The higher the ratio, the better the results. The ratio would be higher before the stall region as the wing produces maximum lift but after the stall, the drag becomes dominant and increases the turbulence at higher angles. The lift-to-drag ratio of lower Reynolds numbers (108000, 125000, 144000, 157000) are more precise than the higher Reynolds number but that does not illustrate the high Reynolds number graphs are inaccurate, but discrepancies are higher.

All above graphs are presumably more accurate for low Reynolds numbers variation since the curves are overlapping on each other and percentage errors are also evaluated smaller compared to higher Reynolds number range (*169000 to 219000*). The average error in the coefficient of lift is -23.8538%, in the drag coefficient is -22.540%, in lift-to-drag ratio is -16.2957%.

Due to the limited citation source of the NASA SC(2)-0410 airfoil profile-wing aerodynamics data the available results validity is a question. However, the external airfoiltools software computes the wing's characteristics with numerical method. From that method for 200000 Reynolds number configuration the highest lift coefficient and drag coefficient are ~0.90 and ~0.117 respectively,

which is reasonably closed with our experimental values as lift coefficient is ~0.82 and drag coefficient is ~0.111.[18]

The below figures represent the main phase of the flow visualisation over the swept-back wing model by this experiment, rest of them are in them between transforming flow patterns to one another.
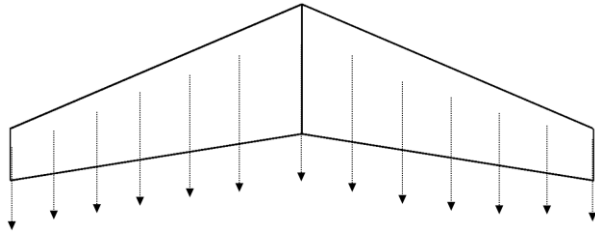
Figure 29: Schematic understanding of the tufts flow visualisation (*straight attached streamlines*)

Figure 30: Tufts attached wing model in wind tunnel (*Re=108000-125000, α =-5° to 3°*)

Figure 31: Schematic understanding of tufts flow visualisation (*wingtip tuft low-frequency oscillation*)
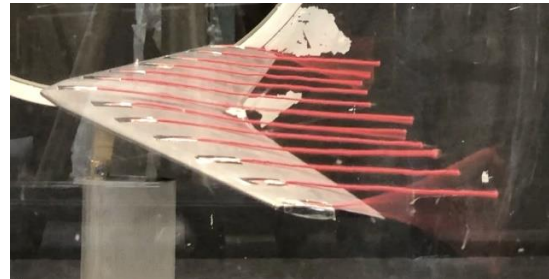
Figure 32: Tufts attached wing model in wind tunnel (*Re=125000-157000, α =-3° to 5°*)

Figure 33: Schematic understanding of tufts flow visualisation (*wingtip tufts high-frequency oscillation*)
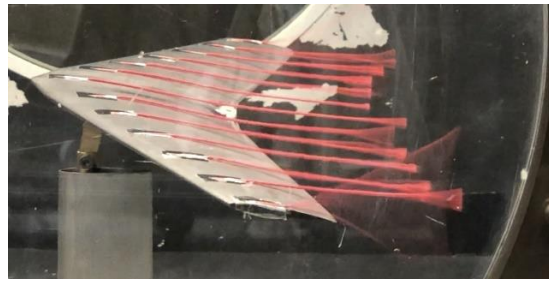
Figure 34: Tufts attached wing model in wind tunnel (*Re=144000-169000, α =3° to 8°*)

Figure 35: Schematic understanding of tufts flow visualisation (*wingtip vortices formation*)
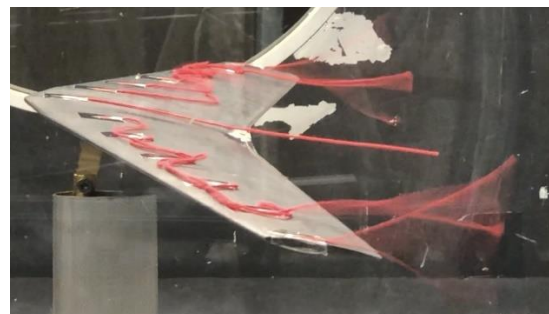
Figure 36: Tufts attached wing model in wind tunnel (*Re=157000-187000, α =5° to 11°*)

Figure 37: Schematic understanding of tufts flow visualisation (*wingtip higher radius vortices formation*)

Figure 38: Tufts attached wing model in wind tunnel (*Re=169000-207000, α =8° to 14°*)
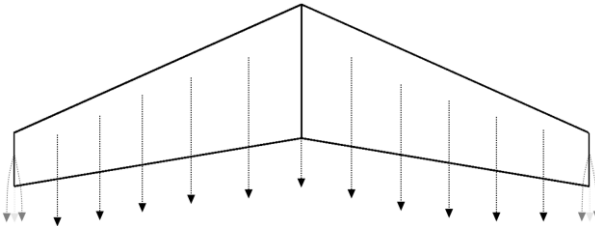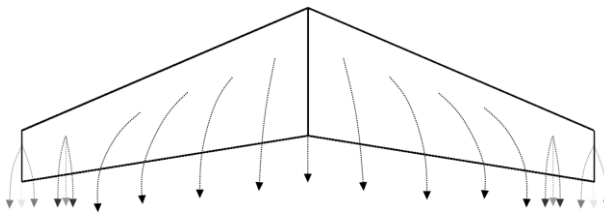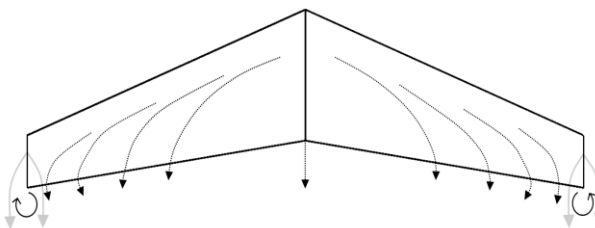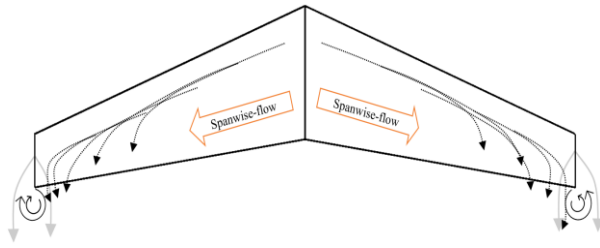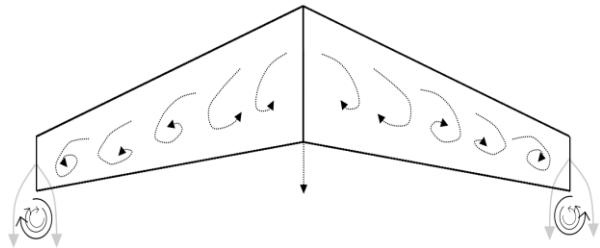

Figure 39: Schematic understanding of tufts flow visualisation (*stalled flow streamlines*)
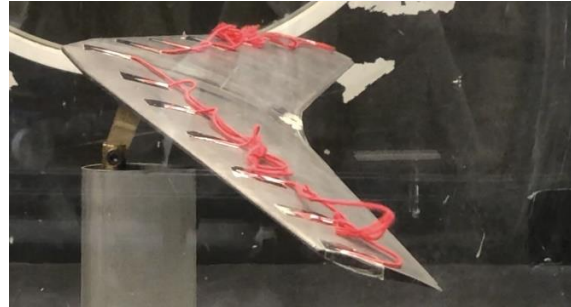
Figure 40: Tufts attached wing model in wind tunnel (*Re=187000-219000, α =12° to 18°*)

The low Reynolds number range (108000 to 125000) at lower angle of attack from -5° to +3° has a flow pattern as illustrate in Figure 30. The effect of sweep will not be in action as the low-speed flow streamlines reach at the leading edge averagely at the same time. Thus, the flow passes over the wing straightly.

Figure 32, is showing the wing at an angle of attack of -3° and +5° with 125,000 to 157,000 Reynolds number range. The flow-streamlines are still attached to the surface of the wing. However, the wing-tip tuft gets started oscillating down-to-up with low frequency that implies the pressure difference initiated between upside and downside of the wing and the behavior is noticed in the Figure 11 where lift coefficient graph enters in the first quadrant.

The oncoming flow-streamlines of 144,000 to 169,000 Reynolds number configuration begin to deviate towards span at the early stage. However, the couple of tufts set at the wingtip oscillate with higher frequency. This behavior suggests an increase in lift and pressure difference values.

Figure 36 suggests the further increment of angle of attack and freestream velocity experiences sweep effect to a great extent as the flow-streamlines started following the wing's leading edge in the short time. The wing tip vortices began to generate with smaller radius at the wing tip. This produces induced drag. The flow-streamlines are still attached to the wing profile.

The values of angle of attack in Figure 38 are +8° to +14° and freestream Reynolds number range is 169000 to 207000. The flow-streamlines move all over across the span of the wing, thus, it now becomes "spanwise flow". At this stage, the flow-streamlines at the edge of separation and lift coefficient value is maximum, also, pressure difference between upper and lower side of the wing

is at the peak due to the highest amount of lift production. The wingtip tufts started rotating with highest radius so the induced drag production at the maximum as well.

From the angle of attack of 12° onwards, either low speeds or high speeds offer stall behavior where flow-streamlines are separated and tufts manner over the wing is disturbed. Stall is the most unstable condition among all above phases since the maneuverability and controllability of an aircraft is a challenge.

There are some values uncounted majorly after 12 degrees because at the higher angle of attack after stall condition, the drag effects are acting robust on the wing and produce great turbulence. During an experiment due to this behavior, the entire wing was lurching. Thus, the experiment was not run for higher angle of attack at high freestream speeds for a safety aspect of an experiment. Therefore, those angle calculations are noted absent in the lift coefficient against angle of attack, drag coefficient against angle of attack and lift-to-drag ratio against angle of attack graphs.

5. CONCLUSION

The objectives of this project are to investigate flow characteristics over the chosen wing model have been successfully fulfilled with various methods of analysis. The empirical results of aerodynamics quantities are satisfactorily validated with computational fluid dynamics methods: non-linear lifting-line theory which is viscous analysis and inviscid analysis by vortex lattice method. The flow streamlines understanding simply developed by tufts-attached modelling. The general flow trends can be demonstrated by increasing freestream Reynolds number and angle of attack makes flow spanwise. At some point, flow patterns are disturbed, and stalls occur. Though some, better workout can be planned out by replacing wing profile model.

5.1 Future Work

Slats and flaps are recommended options to enhance lift- to-drag ratio. By applying these on aircraft's wing, the camber and chord length of the wing can be varied from leading edge-side and trailing edge-side respectively. Moreover, the wing area can also be increased by them. In addition, the camber length increment offers higher lift and flaps upward opening provides drag to aircraft while landing. [21]

Micro-Vortex generators (MVGs) enhance aircraft performance by generating minor vortices. This results in achieving airflow attachment and control flow separation. By applying micro-vortex generators on the wing of the aircraft increases lift to 10%, decreases drag to 50% and increases lift-to-drag ratio 100%. This application improves the overall aerodynamic performance of the aircraft and scales up the aircraft stability and safety cost-effectively. [22]

Figure 41 and Figure 42 are 37° and 40° root to tip sweep, NACA4412 airfoil profile wing models have been run through trial flow analysis in XFLR5. The results of the lift coefficient and drag coefficient estimation are surprisingly improved than the current one. Since, the NACA4412 airfoil has favorable aerodynamic characteristics (i.e., $C_L \sim 1.7$). To determine better flow investigation, the above models can certainly be considered by fabricating these 3D cad wing models in 3D printer and re-conduct an experiment with identical methods by replacing swept back wing profile.
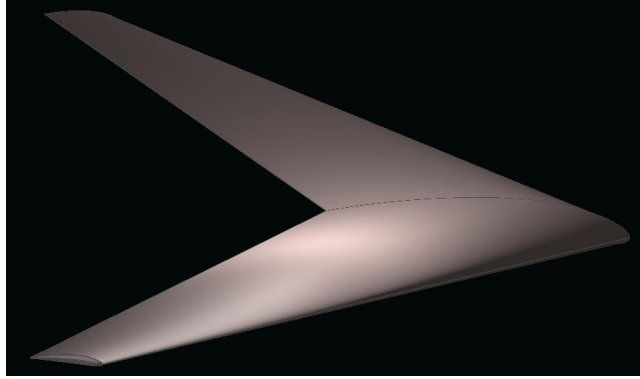
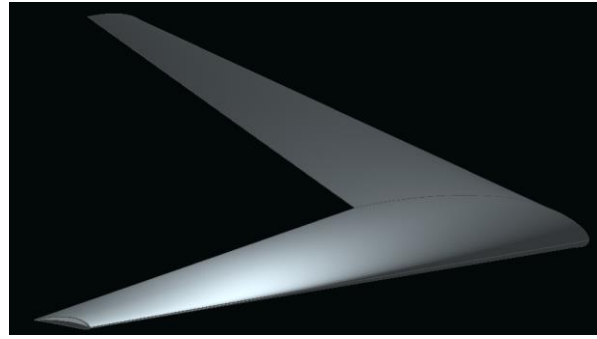Figure 41: 37° swept-back NACA4412 profile wing model (*CAD*)

Figure 42: 40° swept-back NACA4412 profile wing model (*CAD*)

6. REFERENCES

1. Busemann, A. (1937) *Aerodynamic lift at supersonic speeds: Lecture given at the 5th volta conference at Rome*. London: ARC, pp. 210–220.
2. Meier, H. German Development of the Swept Wing 1935–1945, AIAA Library of Flight, 2010
3. Robert T. Jones, "Effects Of Sweep Back On Boundary Layer And Separation," Techinal Report No. 884, 1947
4. Haines, A.B. Some notes on the flow patterns observed over various swept-back wing at low Mach numbers. R&M No. 3192, 1954.
5. Biswas, S., Roy, A., De, P.K., & Majumdar, B. (2020). SAMRIDDHI : A Journal of Physical Sciences, Engineering and Technology, 12(2), 68-71
6. Zhang, S. Experimental investigation of the flow structures over a 40° swept wing (2019), University of Manchester.
7. Takahashi, T. T., Dulin, D. J., & Kady, C. T. (2014). A Method to Allocate Camber, Thickness and Incidence on a Swept Wing. (American Institute of Aeronautics and Astronautics). AIAA 2014-3172.
8. Takahashi, T. T., & Kamat, S. (2015). Revisiting Busemann: The Design Implications of Inconsistencies Found Within Simple Sweep Theory. (American Institute of Aeronautics and Astronautics). AIAA 2015-3376
9. Kirkman, J., (2016), Transonic Flow Around Swept Wings: Revisiting Von Kármán's Similarity Rule, ASU
10. MIT - Massachusetts Institute of Technology , Available at: https://web.mit.edu/hml/ncfmf/05FV.pdf
11. XFLR5 analysis of foils and wings operating at low Reynolds Numbers (2009) Available at: https://engineering.purdue.edu/~aerodyn/AAE333/FALL10/HOMEWORKS/HW13/XFLR5_v6.01_Beta_Win32%282%29/Release/Guidelines.pdf
12. San, K.C., Zong. Y, EFFECTS OF SWEEP ANGLES AND ANGLES OF ATTACK ON JUNCTION-FLOW PATTERNS (2011)

13. Kumar, R., Experimental Study on Flow Characteristics Around Twin Wind blades (2018), Sastra University.
14. The million dollar problem - XFLR5 (no date). Available at: http://www.xflr5.tech/docs/Part%20I:%20Theoretical%20overview.pdf (Accessed: April 25, 2023).
15. Why does a plane fly: The inviscid potential flow - XFLR5 (no date). Available at: http://www.xflr5.tech/docs/Part%20II:%20The%20inviscid%20problem_rev1.1.pdf (Accessed: April 25, 2023).
16. Part IV- theoretical limitations and shortcomings - XFLR5 (no date). Available at: http://www.xflr5.tech/docs/Part%20IV:%20Limitations.pdf (Accessed: April 25, 2023).
17. Jamespkwadhwani and Instructables (2021) Subsonic Wind Tunnel, Instructables. Instructables. Available at: https://www.instructables.com/Subsonic-Wind-Tunnel/ (Accessed: April 25, 2023).
18. *NASA SC(2)-0410 airfoil (SC20410-il)*. Available at: http://airfoiltools.com/airfoil/details?airfoil=sc20410-il#polars (Accessed: April 25, 2023).
19. Carvalho, A.R., (2017) Non-linear lifting-line implementation and validation for aerodynamics and stability analysis
20. Anderson, John D. (2001), Fundamentals of Aerodynamics, p. 360. McGraw-Hill, Boston. ISBN 0-07-237335-0.
21. Flaps and Slats (no date) NASA. NASA. Available at: https://www.grc.nasa.gov/www/k-12/VirtualAero/BottleRocket/airplane/flap.html (Accessed: April 25, 2023).
22. unbar, B. (no date) Micro-vortex generators enhance aircraft performance, NASA. NASA. Available at: https://www.nasa.gov/centers/langley/news/factsheets/Micro-VG.html (Accessed: April 25, 2023).